


CO Multi-line Imaging of Nearby Galaxies (COMING). VI. Radial variations in star formation efficiency

Kazuyuki MURAOKA ^{1,*} Kazuo SORAI,^{2,3,4,5,6} Yusuke MIYAMOTO,⁷ Moe YODA,⁸ Kana MOROKUMA-MATSUI,⁹ Masato I.N. KOBAYASHI,¹⁰ Mayu KURODA,¹ Hiroyuki KANEKO,¹¹ Nario KUNO,^{4,5} Tsutomu T. TAKEUCHI,⁸ Hiroyuki NAKANISHI,¹² Yoshimasa WATANABE,^{4,5} Takahiro TANAKA,⁴ Atsushi YASUDA,⁴ Yoshiyuki YAJIMA,³ Shugo SHIBATA,³ Dragan SALAK,¹³ Daniel ESPADA,^{7,14} Naoko MATSUMOTO,^{7,15} Yuto NOMA,¹³ Shoichiro KITA,⁴ Ryusei KOMATSUZAKI,⁴ Ayumi KAJIKAWA,⁶ Yu YASHIMA,⁶ Hsi-An PAN,¹⁶ Nagisa OI,¹⁷ Masumichi SETA,¹³ and Naomasa NAKAI¹³

¹Department of Physical Science, Osaka Prefecture University, 1-1 Gakuen, Sakai, Osaka 599-8531, Japan

²Department of Physics, Faculty of Science, Hokkaido University, Kita 10, Nishi 8, Kita-ku, Sapporo, Hokkaido 060-0810, Japan

³Department of Cosmosciences, Graduate School of Science, Hokkaido University, Kita 10, Nishi 8, Kita-ku, Sapporo, Hokkaido 060-0810, Japan

⁴Graduate School of Pure and Applied Sciences, University of Tsukuba, 1-1-1 Tennodai, Tsukuba, Ibaraki, 305-8571, Japan

⁵Tomonaga Center for the History of the Universe, University of Tsukuba, 1-1-1 Tennodai, Tsukuba, Ibaraki 305-8571, Japan

⁶Department of Physics, School of Science, Hokkaido University, Kita 10, Nishi 8, Kita-ku, Sapporo, Hokkaido 060-0810, Japan

⁷National Astronomical Observatory of Japan, 2-21-1 Osawa, Mitaka, Tokyo 181-8588, Japan

⁸Division of Particle and Astrophysical Science, Nagoya University, Furo-cho, Chikusa-ku, Nagoya, Aichi 464-8602, Japan

⁹Institute of Space and Astronautical Science, Japan Aerospace Exploration Agency, 3-1-1 Yoshinodai, Chuo-ku, Sagami-hara, Kanagawa 252-5210, Japan

¹⁰Department of Earth and Space Science, Graduate School of Science, Osaka University, 1-1 Machikaneyama-cho, Toyonaka, Osaka 560-0043, Japan

¹¹Nobeyama Radio Observatory, Minamimaki, Minamisaku, Nagano 384-1305, Japan

¹²Graduate School of Science and Engineering, Kagoshima University, 1-21-35 Korimoto, Kagoshima, Kagoshima 890-0065, Japan

¹³Department of Physics, School of Science and Technology, Kwansai Gakuin University, Gakuen 2-1, Sanda, Hyogo 669-1337, Japan

¹⁴The Graduate University for Advanced Studies (SOKENDAI), 2-21-1 Osawa, Mitaka, Tokyo 181-0015, Japan

¹⁵The Research Institute for Time Studies, Yamaguchi University, 1677-1 Yoshida, Yamaguchi, Yamaguchi 753-8511, Japan

¹⁶Academia Sinica, Institute of Astronomy and Astrophysics, No.1, Sec. 4, Roosevelt Rd, Taipei 10617, Taiwan

¹⁷Tokyo University of Science, Faculty of Science Division II, Liberal Arts, 1-3 Kagurazaka, Shinjuku-ku, Tokyo 162-8601, Japan

*E-mail: kmuraoka@p.s.osakafu-u.ac.jp

Received 2018 November 1; Accepted 2019 January 30

Abstract

We examined radial variations in molecular-gas based star formation efficiency (SFE), which is defined as star formation rate per unit molecular gas mass, for 80 galaxies selected from the CO Multi-line Imaging of Nearby Galaxies project (Sorai et al. 2019, PASJ, 71, S14). The radial variations in SFE for individual galaxies are typically a factor of 2–3, which suggests that SFE is nearly constant along the galactocentric radius. We found an averaged SFE in 80 galaxies of $(1.69 \pm 1.1) \times 10^{-9} \text{ yr}^{-1}$, which is consistent with Leroy et al. (2008, AJ, 136, 2782) if we consider the contribution of helium to the molecular gas mass evaluation and the difference in the assumed initial mass function between the two studies. We compared SFE among different morphological (i.e., SA, SAB, and SB) types, and found that SFE within the inner radii ($r/r_{25} < 0.3$, where r_{25} is the *B*-band isophotal radius at 25 mag arcsec⁻²) of SB galaxies is slightly higher than that of SA and SAB galaxies. This trend can be partly explained by the dependence of SFE on global stellar mass, which probably relates to the CO-to-H₂ conversion factor through the metallicity. For two representative SB galaxies in our sample, NGC 3367 and NGC 7479, the ellipse of $r/r_{25} = 0.3$ seems to cover not only the central region but also the inner part of the disk, mainly the bar. These two galaxies show higher SFE in the bar than in the spiral arms. However, we found an opposite trend in NGC 4303; SFE is lower in the bar than in the spiral arms, which is consistent with earlier studies (e.g., Momose et al. 2010, ApJ, 721, 383). These results suggest a diversity of star formation activities in the bar.

Key words: galaxies: ISM — galaxies: star formation — ISM: molecules

1 Introduction

Star formation is one of the most fundamental processes in the evolution of galaxies. Stars are formed by the contraction of the molecular interstellar medium, which would be initiated by gravitational instability and/or cloud–cloud collision (e.g., McKee & Ostriker 2007). Thus the observational study of the physical relation between molecular gas and star formation is indispensable in understanding the evolution of galaxies.

The activity of star formation in galaxies is quantified as star formation rate (SFR). Although the surface density of SFR is related to that of molecular gas via a power law (e.g., Kennicutt 1998), its scatter is not so small; at a given surface gas density, the scatter of SFR spreads up to ~ 1 dex even for nearby disk galaxies (e.g., Daddi et al. 2010). In order to understand the physical origin of such a scatter, star formation efficiency (SFE), which is defined as SFR per unit molecular gas mass, is often investigated. Many earlier studies pointed out that SFE differs among galaxies and even within a galaxy. For example,

Young et al. (1996) reported that galaxies in disturbed environments (i.e., strongly interacting systems) show about four times higher SFE than isolated spiral galaxies. Lisensfeld et al. (2011) confirmed that SFE is a factor of 5 higher for a strongly perturbed sample and about 2 higher for a weakly perturbed sample compared to isolated galaxies. For an individual galaxy, Muraoka et al. (2007) found that SFE is four times higher in the central region than in the disk of the barred spiral galaxy M 83. In addition, some earlier studies toward nearby galaxies reported that SFE is lower in bars than in the spiral arms (e.g., Momose et al. 2010; Watanabe et al. 2011; Hirota et al. 2014; Yajima et al. 2019).

An extensive study of spatially-resolved SFE in galaxies has been conducted by Leroy et al. (2008). They measured SFE at 800-pc resolution in 23 nearby galaxies using HERA CO-Line Extragalactic Survey (HERACLES) data, and found that SFE based on H₂ is nearly constant at $(5.25 \pm 2.5) \times 10^{-10} \text{ yr}^{-1}$ as a function of various variables; i.e., galactocentric radius, stellar mass surface density, gas surface density, free-fall and orbital timescales,

midplane gas pressure, stability of the gas disk to collapse, the ability of perturbations to grow despite shear, and the ability of a cold phase to form, in H_2 -dominated inner parts of spiral galaxies. A similar trend is reported by Bigiel et al. (2011); they found a roughly constant molecular-gas depletion time, which is the inverse of SFE, of ~ 2.35 Gyr (corresponding to SFE of $4.26 \times 10^{-10} \text{ yr}^{-1}$) at 1-kpc resolution in the HERACLES sample. Recently, Utomo et al. (2017) investigated the variation in molecular-gas depletion time on kpc-scales in 52 galaxies based on the EDGE-CALIFA survey. They found that 14 galaxies show a shorter depletion time of ~ 1 Gyr (i.e., SFE of 10^{-9} yr^{-1}) in the center relative to that in the disk, ~ 2.4 Gyr (SFE of $4.2 \times 10^{-10} \text{ yr}^{-1}$). They also found that the central increase in SFE is correlated with a central increase in the stellar surface density, suggesting that a higher SFE is associated with molecular gas compression by the stellar gravitational potential.

Currently, 147 $\text{CO}(J = 1-0)$ maps of nearby galaxies, which are obtained by the CO Multi-line Imaging of Nearby Galaxies (COMING) project (Sorai et al. 2019), have been available. COMING is a project to map $J = 1-0$ emission of ^{12}CO , ^{13}CO , and C^{18}O molecules toward a 70% area of the optical disks of nearby galaxies using the FOur-beam REceiver System on the 45 m Telescope (FOREST: Minamidani et al. 2016) at the Nobeyama Radio Observatory (NRO). Utilizing the initial CO data of COMING, the quantitative relationship between molecular gas and star formation has been examined for individual galaxies; NGC 2903 (Muraoka et al. 2016), NGC 2976 (Hatakeyama et al. 2017), and NGC 4303 (Yajima et al. 2019). In particular, a positive correlation between SFE and molecular gas density is reported (Muraoka et al. 2016; Yajima et al. 2019).

We extend the study of the relation between molecular gas and star formation to much of the COMING sample. In particular, we focus on the difference in SFE both among galaxies and within each galaxy. As a first step, we investigate radial variations in SFE of the COMING sample. Since COMING is the largest $\text{CO}(J = 1-0)$ imaging survey of nearby galaxies, we can obtain the *general* trend of variations in SFE with less bias.

The structure of this paper is as follows. In section 2, we describe the selection of target galaxies and the data utilized to calculate SFE. Then, we explain the derivation of radial profiles of SFE in subsection 3.1, and show the results and their comparison to earlier studies in subsection 3.2. In section 4, we first examine the dependence of SFE on the global stellar mass. In addition, we investigate the difference in SFE among different morphological types of galaxies, i.e., SA, SAB, and SB galaxies. Finally, we provide some implications regarding star formation in the inner part of disk galaxies; in particular, star formation in the bar.

2 Sample selection and data

In this section, we describe selection criteria of sample galaxies from COMING and summarize the data utilized to calculate SFE.

2.1 Sample selection

In order to select appropriate galaxies for examining radial variations in SFE from the COMING sample, we set three criteria as follows. (1) The inclination (i) is less than 75° . (2) The obvious interaction of galaxies is not observed. (3) SFR can be calculated by a combination of GALEX far-ultraviolet (FUV) (Gil de Paz et al. 2007) and WISE $22 \mu\text{m}$ (Wright et al. 2010) data. The first criterion is set because it is difficult to derive accurately azimuthally-averaged radial profiles of molecular gas mass and SFR toward highly-inclined galaxies. The second is set to avoid enhancement or suppression of star formation by the interaction of galaxies. The third is to obtain homogeneous SFR maps among selected galaxies, and to discuss the difference in SFE without systematic errors caused by different calibration methods of SFR. Note that we did not employ Multiband Imaging Photometer for Spitzer $24 \mu\text{m}$ data as a tracer of SFR because the number of corresponding $24 \mu\text{m}$ maps for the COMING sample is smaller than that of WISE $22 \mu\text{m}$ maps and because some $24 \mu\text{m}$ maps suffer from saturation in bright regions.

Based on the three criteria, we finally selected 80 galaxies from the COMING sample in total; 30 SA, 33 SAB, and 17 SB galaxies. Parameters for the 80 selected galaxies, i.e., galaxy name, B -band isophotal radius at 25 mag arcsec $^{-2}$ (r_{25}), inclination i , position angle (P.A.), and global stellar mass (M_*), are summarized in table 1. Figure 1 shows histograms of M_* for the three galaxy types. Compared to SA and SAB galaxies, selected SB galaxies are less massive. This trend also appears in the original COMING sample (Sorai et al. 2019).

2.2 Data

We produce maps of the H_2 mass surface density Σ_{H_2} and the SFR surface density Σ_{SFR} to obtain radial profiles of SFE for selected galaxies.

2.2.1 H_2 mass

Σ_{H_2} is calculated from $^{12}\text{CO}(J = 1-0)$ integrated intensities obtained by COMING at an angular resolution of $17''$, which corresponds to the spatial resolution of 0.3–3 kpc (typically ~ 1.5 kpc) for our sample. A detailed description of the COMING observations, data processing, and CO maps are presented in the COMING overview paper (Sorai

Table 1. Parameters of selected SA, SAB, and SB galaxies.*

Galaxy	r_{25} (')	i (°)	P.A. (°)	$\log M_*$ (M_\odot)
— SA galaxies —				
NGC 470	1.41	58.0	155.4	10.73
NGC 628	5.24	7	20	10.25
NGC 1084	1.62	57.2	-141.6	10.58
NGC 1482	1.23	55.2	-61.5	10.31
NGC 2742	1.51	59.9	-93.5	10.42
NGC 2748	1.51	72.8	-138.8	10.12
NGC 2775	2.14	35.4	163.5	10.71
NGC 2841	4.07	73.7	152.6	10.90
NGC 2967	1.51	16.5	64.0	10.21
NGC 2976	2.95	64.5	-25.5	9.14
NGC 3147	1.95	35.2	142.79	11.27
NGC 3169	2.19	39.0	-123.7	10.89
NGC 3338	2.95	60.9	97.1	10.48
NGC 3370	1.58	55.1	-38.1	10.09
NGC 3655	0.78	23.5	-100.3	10.68
NGC 3672	2.09	67.2	7.8	10.63
NGC 3675	2.95	67.8	176	10.89
NGC 3810	2.14	42.2	-154.3	10.33
NGC 3813	1.12	68.2	83.1	10.26
NGC 3938	2.69	20.9	-154.0	10.43
NGC 3949	1.44	52.9	-58.2	10.20
NGC 4030	2.09	39.0	29.6	11.08
NGC 4041	1.35	23.4	-138.7	10.68
NGC 4632	1.55	65.9	60.5	9.70
NGC 4750	1.02	40.0	-50	10.62
NGC 5364	3.38	47.9	-144.4	10.45
NGC 5676	1.99	59.8	-131.9	10.94
NGC 6503	3.54	73.5	-60.2	9.68
NGC 7625	0.79	37.4	-151.4	10.19
NGC 7721	1.78	69.8	-164.2	10.41
— SAB galaxies —				
NGC 157	2.09	48.0	-136	10.16
NGC 1087	1.86	50.5	1.4	10.00
NGC 2268	1.62	58	-112	10.62
NGC 2276	1.41	48	-113	10.87
NGC 2715	2.45	67.8	-159.1	10.01
NGC 2903	6.30	67	-155	10.61
NGC 3166	2.40	55.7	-100.4	10.78
NGC 3310	1.55	56	150	9.83
NGC 3344	3.54	27.0	-37.3	10.08
NGC 3368	3.80	57.5	169.0	10.52
NGC 3437	1.26	65.9	-61.5	10.29
NGC 3627	4.56	52	176	10.60
NGC 3888	0.87	41.8	121.2	10.53
NGC 3893	2.24	30	-13	10.29
NGC 4045	1.35	48.4	-92.1	10.63
NGC 4088	2.88	68.9	-126.8	10.39
NGC 4258	9.31	72	-29	10.55
NGC 4303	3.23	27.0	-36.4	10.77
NGC 4433	1.10	64	5	10.63
NGC 4527	3.09	70	69.5	10.69
NGC 4536	3.80	64.2	-54.5	10.46
NGC 4559	5.36	63.1	-36.8	9.68
NGC 4579	2.95	41.7	92.1	10.84

Table 1. (Continued)

Galaxy	r_{25} (')	i (°)	P.A. (°)	$\log M_*$ (M_\odot)
— SAB galaxies —				
NGC 4602	1.70	67.9	100.7	10.75
NGC 4666	2.29	70	-135	10.57
NGC 4818	2.14	67.2	-175.5	9.94
NGC 5005	2.88	66.7	67.0	10.92
NGC 5248	3.09	38.6	103.9	10.37
NGC 5665	0.96	51.7	154.7	9.79
NGC 5678	1.66	56.9	-177.5	10.89
NGC 5713	1.38	33	-157	10.30
NGC 6574	0.71	45	165	10.97
NGC 6951	1.95	30	135	10.87
— SB galaxies —				
NGC 150	1.95	59.3	108.9	10.42
NGC 337	1.44	44.5	119.6	9.95
NGC 660	4.16	72	-138.5	10.44
NGC 701	1.23	58.6	44.7	10.02
NGC 1022	1.20	30	85	10.18
NGC 1530	2.29	45	-172	10.42
NGC 2633	1.23	50.1	-176.3	10.41
NGC 3198	4.26	71.5	-145.0	10.13
NGC 3351	3.71	41	-168	10.39
NGC 3359	3.62	51	-8	10.30
NGC 3367	1.26	30	51	10.50
NGC 3583	1.41	38.6	131.3	10.54
NGC 3686	1.62	35.2	19.5	10.01
NGC 4605	2.88	69	-67	9.40
NGC 5792	3.46	64	-98.5	10.93
NGC 7479	2.04	51	-158	11.03
NGC 7798	0.69	31.9	70.5	10.30

All the parameters are based on Sorai et al. (2019). They estimated M_ based on the WISE 3.4 μm band infrared luminosity (Wen et al. 2013).

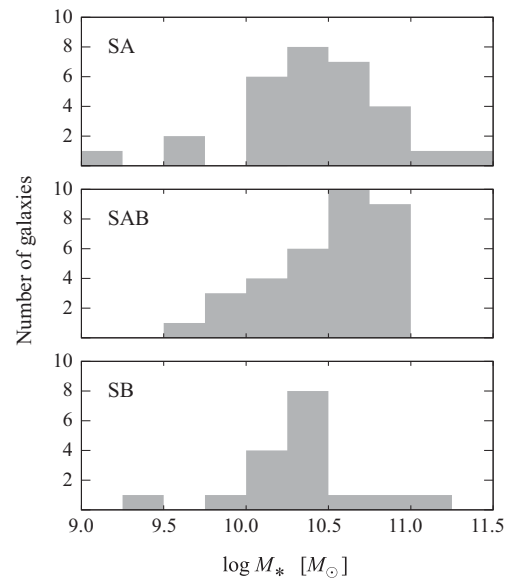


Fig. 1. Histograms of stellar mass M_* for selected SA, SAB, and SB galaxies. There are few SB galaxies with M_* of more than $10^{10.5} M_\odot$.

et al. 2019). We uniformly assume the standard CO-to-H₂ conversion factor $X_{\text{CO}} = 2.0 \times 10^{20} \text{ cm}^{-2} (\text{K km s}^{-1})^{-1}$ (Bolatto et al. 2013) for all the selected galaxies. In addition, no spatial variation in X_{CO} is assumed within each galaxy. Using a factor of $\cos(i)$, Σ_{H_2} values are corrected (i.e., deprojected) for each galaxy. Note that the contribution of helium mass (a factor of 1.36) is *not* included in our Σ_{H_2} .

2.2.2 Star formation rate

Σ_{SFR} is calculated from a linear combination of GALEX FUV and WISE 22 μm intensities using the following formula (Casasola et al. 2017):

$$\left[\frac{\Sigma_{\text{SFR}}}{M_{\odot} \text{ yr}^{-1} \text{ kpc}^{-2}} \right] = \left[3.2 \times 10^{-3} \left(\frac{I_{22}}{\text{MJy sr}^{-1}} \right) + 8.1 \times 10^{-2} \left(\frac{I_{\text{FUV}}}{\text{MJy sr}^{-1}} \right) \right] \times \cos i \times 1.59, \quad (1)$$

where I_{22} and I_{FUV} are 22 μm and FUV intensities, respectively. A factor of 1.59 converts the obtained Σ_{SFR} to those shown by Kennicutt (1998) assuming the truncated Salpeter (1955) initial mass function (IMF).

For FUV data, we firstly estimated the Galactic dust extinction at 1538.6 \AA , which is the effective wavelength of FUV band, based on the Galactic V-band extinction A_V (Schlafly & Finkbeiner 2011) and Cardelli, Clayton, and Mathis (1989) model, and corrected the dust extinction. Then, we convolved the FUV images at an angular resolution of 4".2 to 17" to match COMING data. Finally, we converted the unit of the original FUV images, count pixel second (CPS), into MJy sr^{-1} .

For WISE 22 μm data, we individually determined the background level as an average of the intensity value at the blank sky, and subtracted it. Then, we converted the unit of original 22 μm images, digital number, into MJy sr^{-1} . Note that we did not convolve 22 μm images because the effective angular resolution of the 22 μm atlas images is 16".8 (R. M. Cutri et al. 2012),¹ which is almost the same as that of the COMING data.

We finally obtained the SFR map with an angular resolution of 17". The details of treating FUV and 22 μm data and calculating Σ_{SFR} are described in M. Yoda et al. (in preparation).

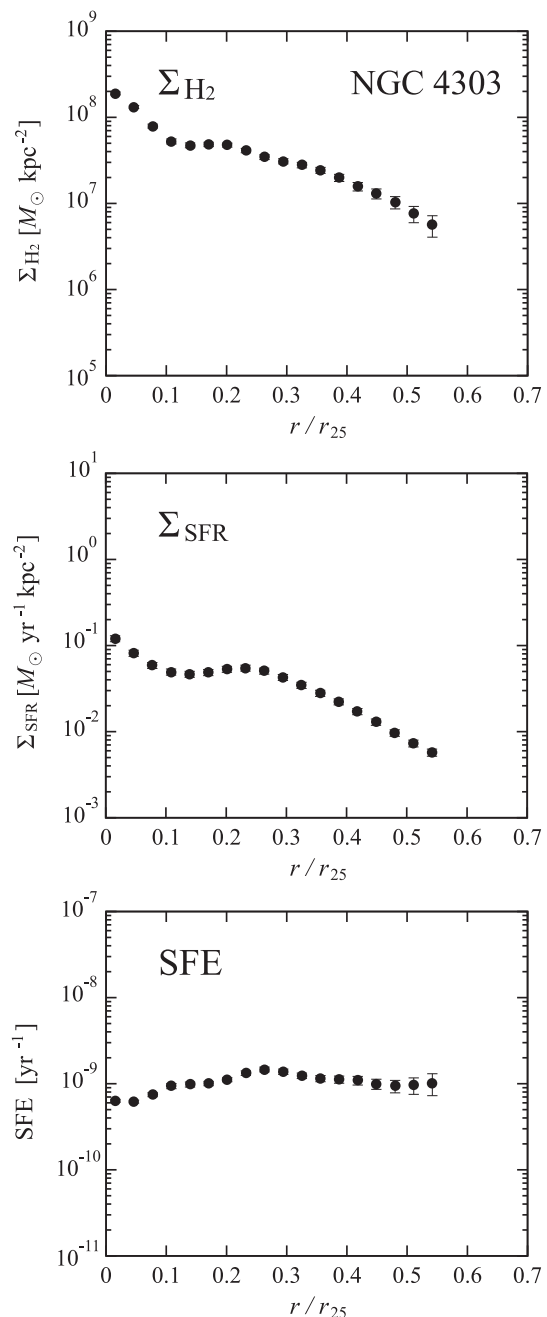


Fig. 2. Example of radial profiles of Σ_{H_2} (top), Σ_{SFR} (middle), and SFE (bottom) for NGC 4303.

3 Radial profiles of SFE

3.1 Derivation of radial profiles

Using the maps of Σ_{H_2} and Σ_{SFR} , we obtain radial profiles of SFE as described below. First, both maps with a grid size of 6" per pixel are regridded to 1".2 per pixel. Secondly, we determine a tilted ring of a galaxy based on its position angle and inclination. Then, we set 6"-wide tilted rings as bins of a radial profile, and calculated azimuthally-averaged Σ_{H_2} and Σ_{SFR} in each bin. Finally, SFE in each

¹ Cutri, R. M., et al. 2012, Explanatory Supplement to the WISE All-Sky Data Release Products (<http://wise2.ipac.caltech.edu/docs/release/allsky/expsup/>).

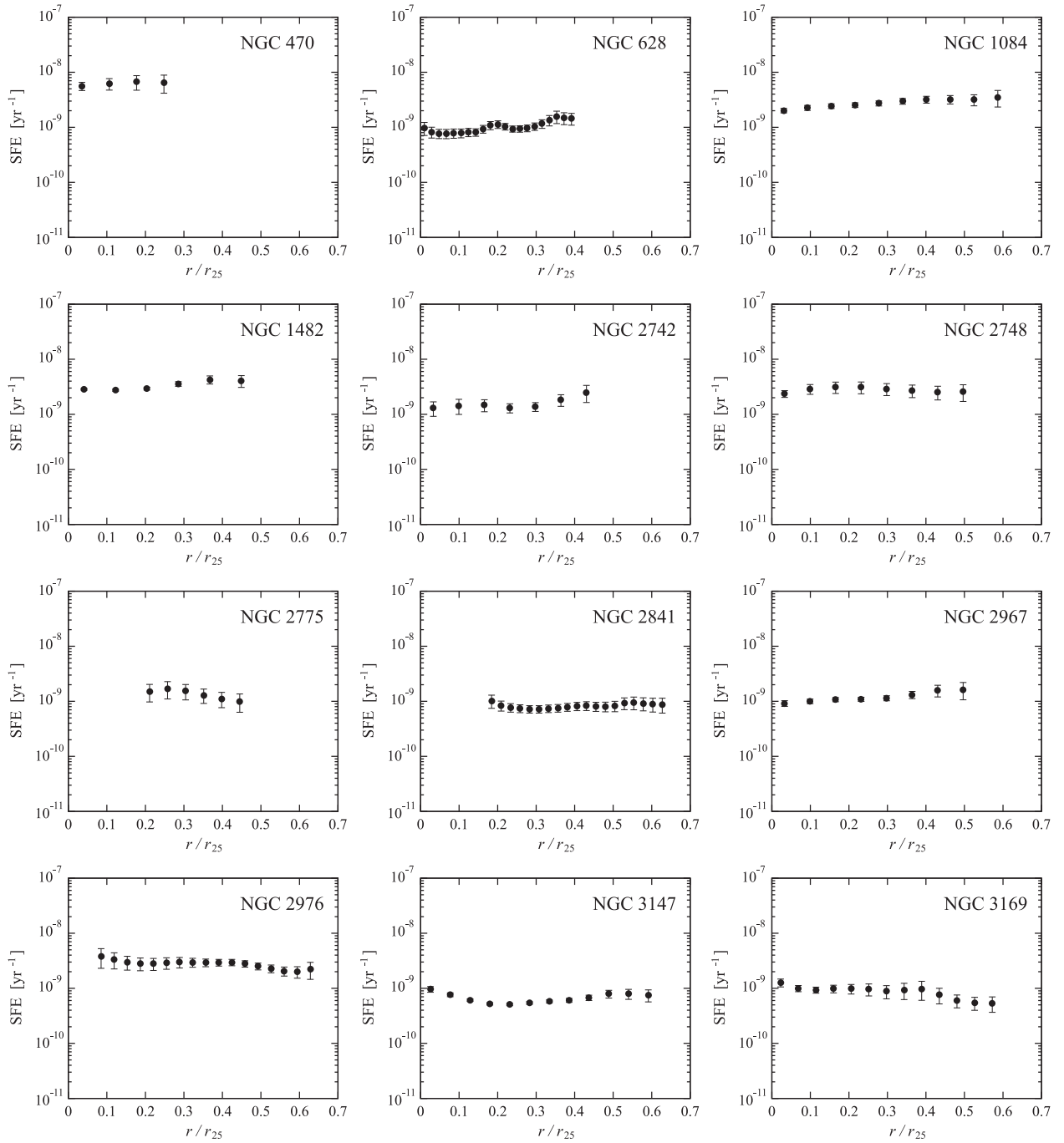


Fig. 3. SFE as a function of the galactocentric radius in the unit of r/r_{25} for individual SA galaxies.

bin is obtained by the division of $\Sigma_{\text{SFR}}/\Sigma_{\text{H}_2}$. We normalize the unit of galactocentric radius by r_{25} , and thus we show SFE as a function of r/r_{25} . For barred spiral (SAB and SB) galaxies, the bar-end roughly corresponds to r/r_{25} values of 0.2–0.3.

We treated the uncertainties in Σ_{H_2} , Σ_{SFR} , and SFE for each bin in the manner of Leroy et al. (2008). They took the uncertainty σ in a quantity averaged over a tilted ring

to be

$$\sigma = \frac{\sigma_{\text{rms}}}{\sqrt{N_{\text{pix,ring}}/N_{\text{pix,beam}}}}, \quad (2)$$

where σ_{rms} is the rms scatter within the tilted ring, $N_{\text{pix,ring}}$ is the number of pixels included in the ring, and $N_{\text{pix,beam}}$ is the number of pixels included in the observing beam size. However, the obtained σ for Σ_{SFR} seemed too small

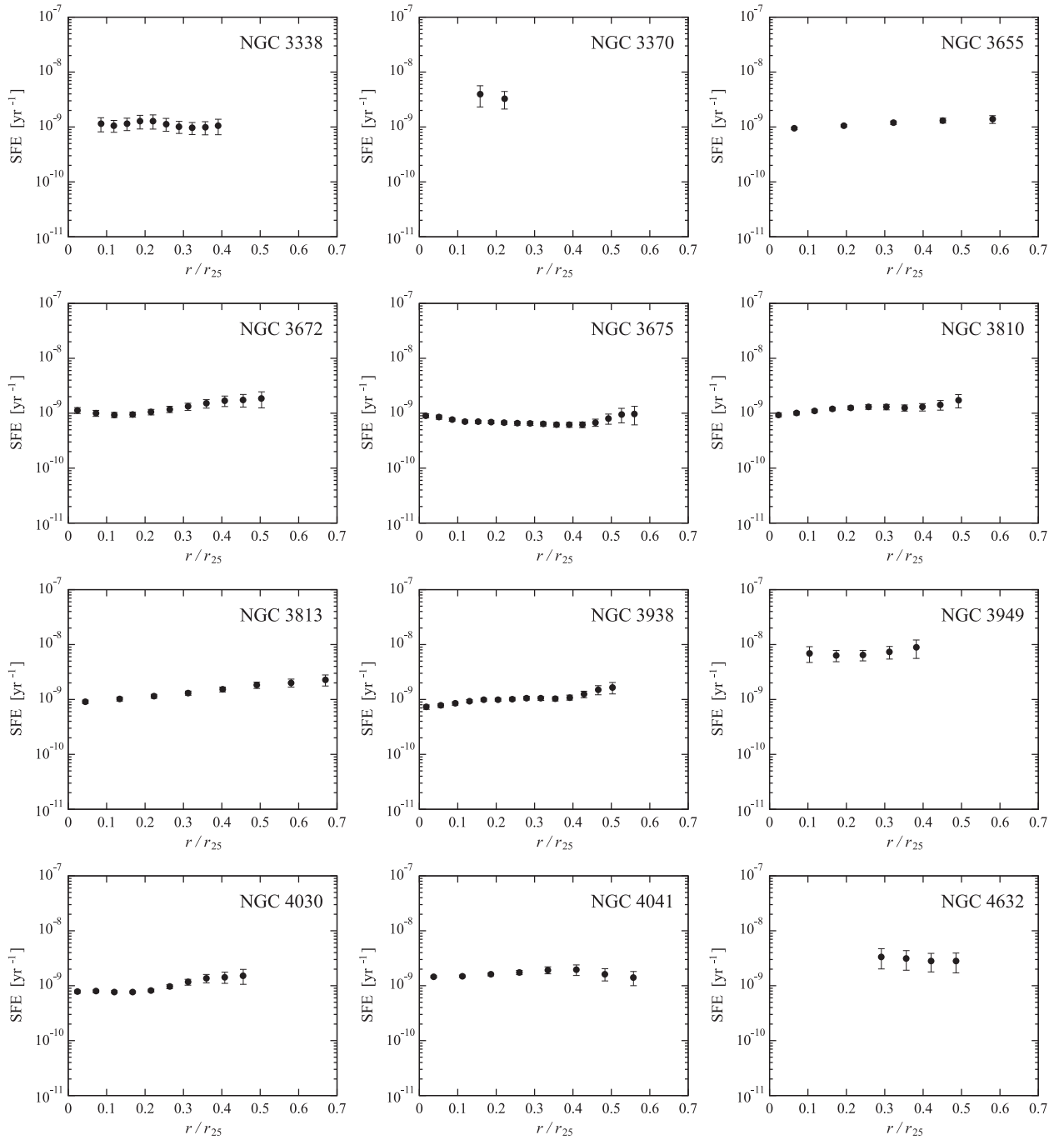


Fig. 3. (Continued)

(typically $<1\%$), and thus we considered the systematic uncertainties as σ for Σ_{SFR} . According to Gil de Paz et al. (2007), the error in the FUV zero-point calibration is estimated to be 0.15 mag, which yields the uncertainty of $\sim 15\%$. In addition, Jarrett et al. (2011) reported that the rms scatter about the zero level is 5.7% for the WISE $22\ \mu\text{m}$ band. Considering that the WISE $22\ \mu\text{m}$ intensity is dom-

inant in Σ_{SFR} (typically $>80\%$) compared to FUV intensity, we estimated that the systematic uncertainty of Σ_{SFR} is typically 8%.

We calculated σ of Σ_{H_2} and the systematic uncertainty of Σ_{SFR} in each bin, and finally derived the uncertainty in SFE from the error propagation. Figure 2 shows an example of radial profiles of Σ_{H_2} , Σ_{SFR} , and SFE for NGC 4303. We

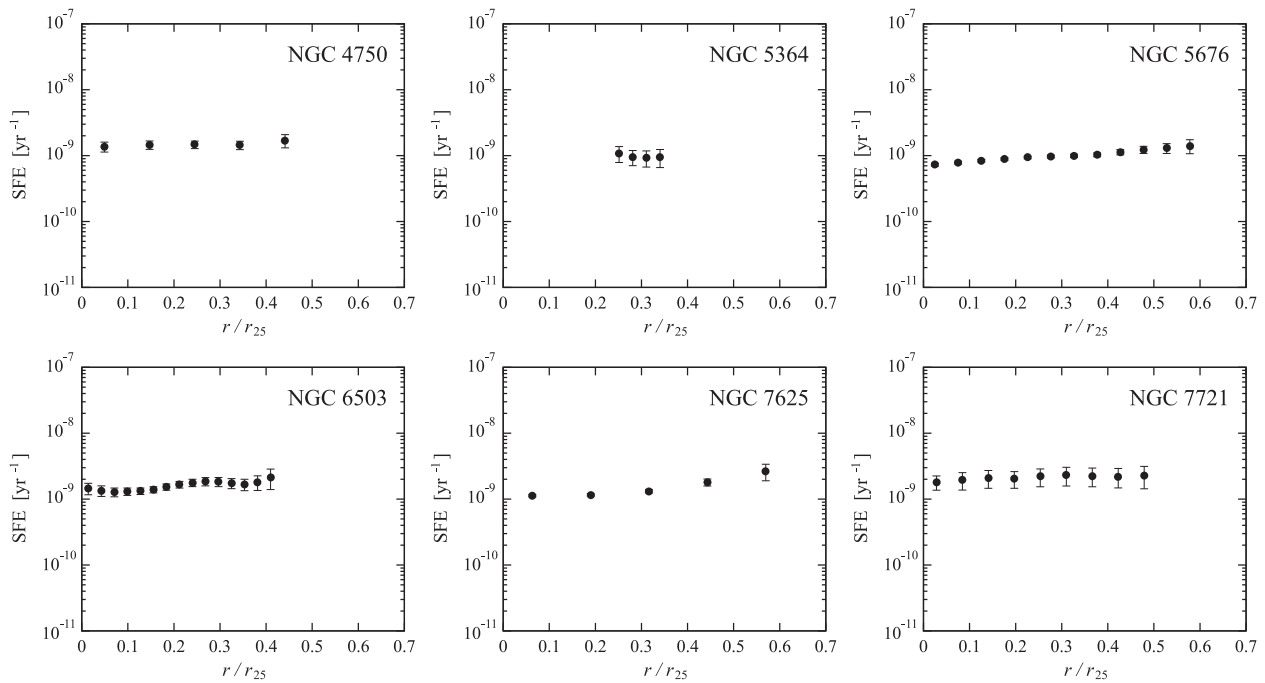


Fig. 3. (Continued)

display each measurement (data point) in bins where the calculated SFE is more than 3σ .

3.2 Results

Figures 3, 4, and 5 show the radial profiles of SFE for individual SA, SAB, and SB galaxies, respectively. Most of the galaxies do not show drastic variations in SFE except for three barred spiral galaxies (NGC 1087, NGC 2268, and NGC 4579); the radial variation in SFE is less than a factor of 5 (typically a factor of 2–3). This suggests that molecular-gas based SFE is nearly constant along galactocentric radius (see also figures 6 and 7), which is consistent with the finding by Leroy et al. (2008).

We found an averaged SFE in 80 galaxies of $(1.69 \pm 1.1) \times 10^{-9} \text{ yr}^{-1}$, which seems significantly higher than that of $(5.25 \pm 2.5) \times 10^{-10} \text{ yr}^{-1}$ reported by Leroy et al. (2008). This is because there are two differences in the calculation of SFE between the two studies; first, the contribution of helium mass (a factor of 1.36) is not included in our Σ_{H_2} . In addition, our Σ_{SFR} is systematically higher than that in Leroy et al. (2008) by a factor of 1.59 because they assumed a Kroupa (2001) IMF. Therefore, our SFE must be divided by 2.16 when it is compared with the SFE in Leroy et al. (2008). This yields an averaged SFE of $(7.82 \pm 5.0) \times 10^{-10} \text{ yr}^{-1}$ in this study, which is consistent with that of Leroy et al. (2008) within the error ranges.

In figure 4, NGC 3310 shows an extremely high SFE ($>10^{-8} \text{ yr}^{-1}$). This is partly because of an intense star-

burst likely caused by a recent minor interaction (Miralles-Caballero et al. 2014), which yields an elevated SFR. In addition, NGC 3310 shows a moderately low metallicity ($0.2\text{--}0.4 Z_{\odot}$; Pastoriza et al. 1993), which suggests higher X_{CO} than the standard value and thus the underestimation of Σ_{H_2} . For these reasons, such an extremely high SFE is observed in NGC 3310.

4 Discussion

In this section, we examine the general trend of radial variations in SFE for each galaxy type, i.e., SA, SAB, and SB galaxies. Then, we evaluate its difference among the three types. In particular, we discuss an unexpected trend of SFE; i.e., higher SFE within the inner radii of SB galaxies compared to SA and SAB galaxies.

4.1 General trend of SFE and its dependence on global stellar mass

Figure 6 shows the compiled radial profiles of SFE for each galaxy type. As described in subsection 3.2, SFE seems nearly constant along galactocentric radius. In order to evaluate how radial profiles are affected by the difference in spatial resolution among our sample, we examined radial profiles of SFE at a common spatial resolution of 3 kpc as shown in figure 7. Radial profiles shown in figures 6 and 7 seem closely similar to each other, and thus we concluded

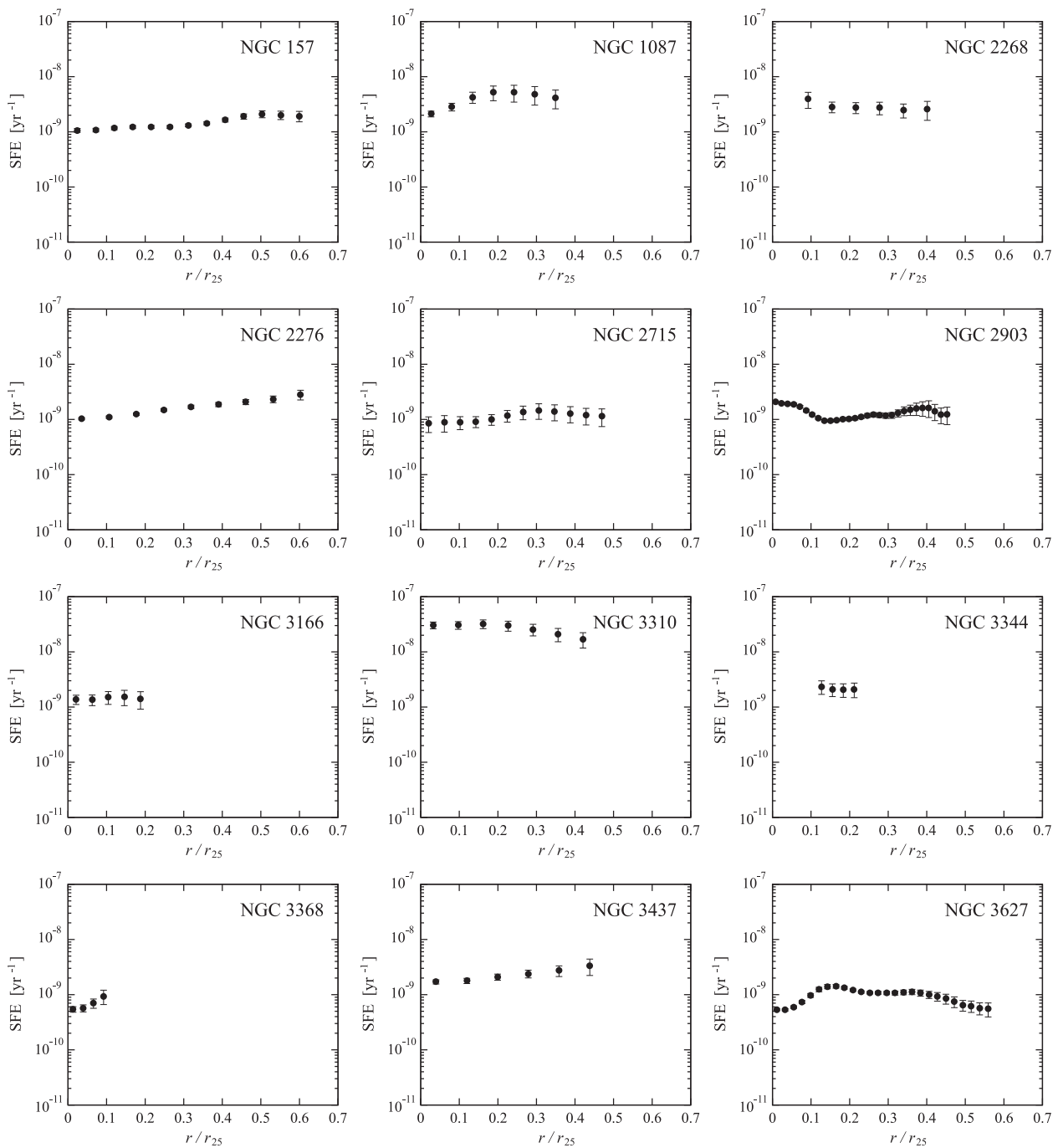


Fig. 4. SFE as a function of the galactocentric radius in the unit of r/r_{25} for individual SAB galaxies.

that the difference in spatial resolution does not affect the subsequent discussion.

We found a possibility that SFE in the inner radii of SB galaxies is higher than that of SA and SAB galaxies. To confirm this trend clearly, we examine averaged SFE over a $0.1r/r_{25}$ width for every galaxy type as shown in figure 8. In the inner radii ($r/r_{25} < 0.3$), the SFE of SB galaxies ($>2.0 \times 10^{-9} \text{ yr}^{-1}$) is slightly higher than that of SA and SAB galaxies ($\sim 1.4 \times 10^{-9} \text{ yr}^{-1}$). On the other

hand, in the outer radii ($0.3 < r/r_{25} < 0.5$), all the three types show similar SFEs of $(1.3\text{--}1.7) \times 10^{-9} \text{ yr}^{-1}$. Note that the number of data points for SB galaxies in figure 6 is smaller than for SA and SB galaxies due to the difference in sample size. This might cause the averaged radial profile for SB galaxies to deviate from other types. In particular, such a deviation seems evident in the outermost radii ($r/r_{25} > 0.5$); SFE of SB galaxies becomes slightly higher than SA and SAB galaxies again at the radii, whereas this trend

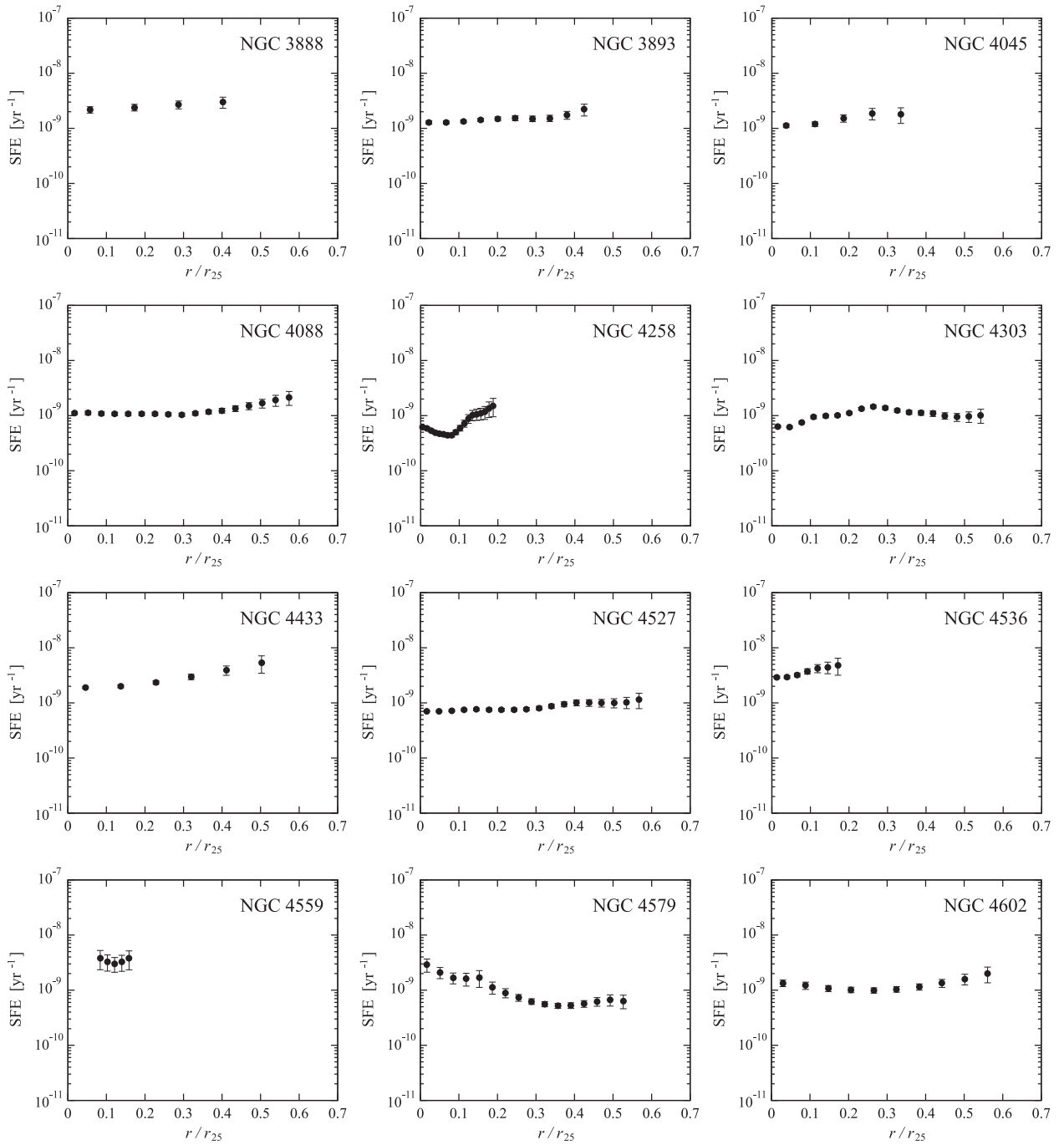


Fig. 4. (Continued)

seems doubtful because there are few data points as shown in figure 6. Such an effect due to the difference in sample size is also discussed in subsection 4.2.

Here, we investigate why SB galaxies show higher SFE within the inner radii ($r/r_{25} < 0.3$) compared to SA and SAB galaxies. First, we examine the dependence of SFE on global stellar mass M_* because selected SB galaxies in this study are less massive compared to SA and SAB galaxies, as described in subsection 2.1. Figure 9 shows the comparison between

SFE within the inner radii and M_* in our sample. A trend that SFE decreases with the increase in M_* can be seen. We obtain a Spearman rank correlation coefficient of -0.52 for this $\log \text{SFE} - \log M_*$ relation, suggesting a significant negative correlation. Such a negative correlation between SFE and M_* in the stellar mass range of 10^9 to $10^{11.5} M_\odot$ has been reported in earlier studies. For example, Saintonge et al. (2011) and Huang and Kauffmann (2014) found that molecular-gas depletion time becomes longer (i.e. SFE

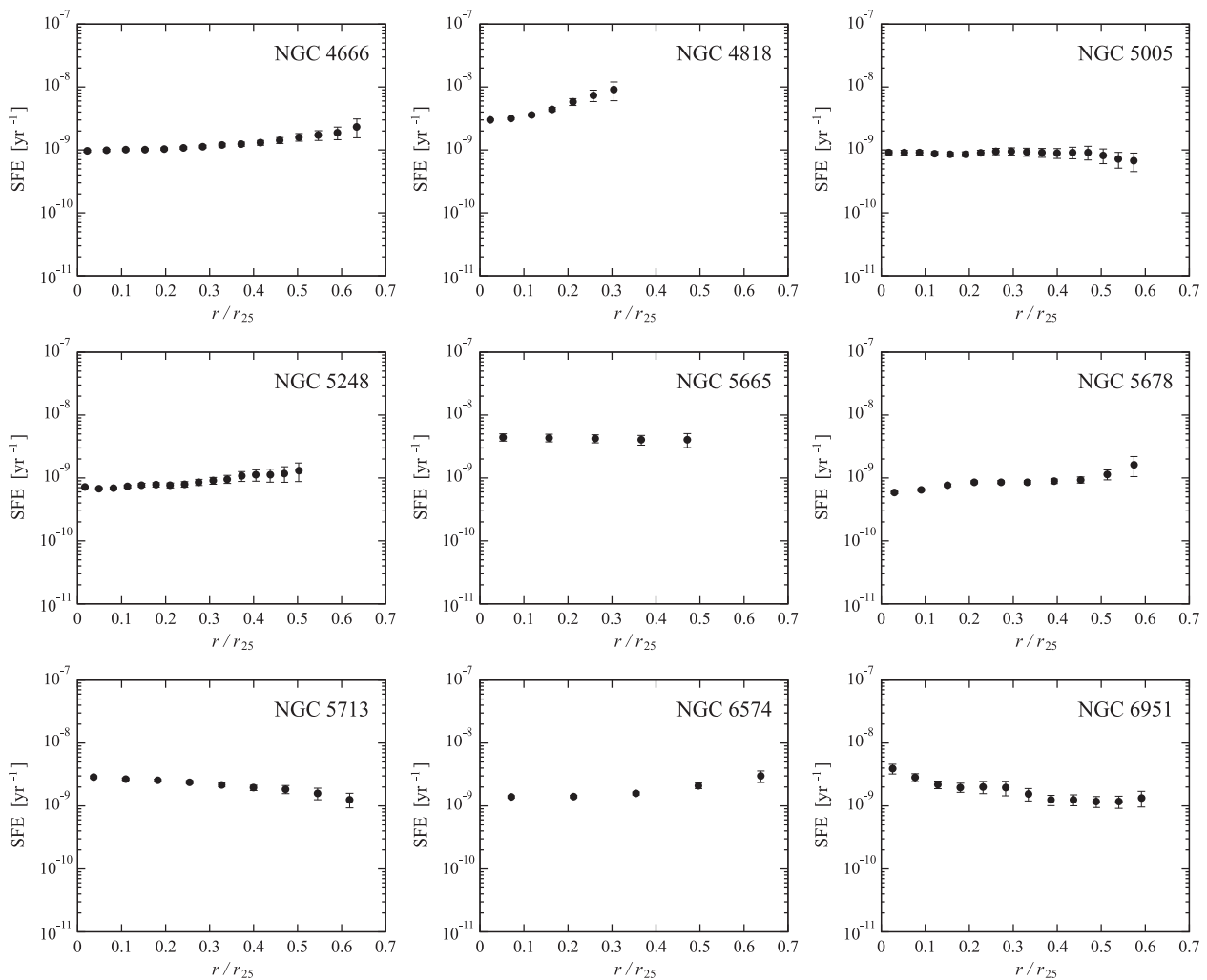


Fig. 4. (Continued)

becomes lower) with an increase in stellar mass based on CO Legacy Database for GALEX Arcibo Sloan Digital Sky Survey. In addition, Leroy et al. (2013) and Boselli et al. (2014) reported similar relationships based on HERACLES and the Herschel Reference Survey, respectively. This correlation is presumably due to the relationship between stellar mass and metallicity, i.e., the so-called mass–metallicity relation (e.g., Lequeux et al. 1979; Tremonti et al. 2004; Hughes et al. 2013). Both parameters can trace the integrated star formation history within a galaxy; star formation firstly increases stellar mass, and then heavy elements are ejected from evolved stars into interstellar space. The increase in metallicity results in a decrease in X_{CO} (e.g., Arimoto et al. 1996). Since we assume the standard X_{CO} for the whole sample, we may overestimate Σ_{H_2} for galaxies with high metallicity, which eventually results in an underestimation of SFE. In this case, a negative correlation between

SFE and M_* may appear. In fact, the negative correlation between SFE and the metallicity is already found (e.g., Dib et al. 2011; Leroy et al. 2013).

Therefore, the obtained negative correlation between SFE and M_* can be interpreted as an apparent variation in SFE due to the difference in X_{CO} among our sample. Such an explanation is also reported by Leroy et al. (2013). However, we cannot rule out another possibility that SFE truly varies depending on galaxy mass. For example, Saintonge et al. (2011) suggest that smaller galaxies have more bursty star formation histories due to minor starburst events, and also suggest that quenching in high-mass galaxies prevent the molecular gas from forming stars without destroying the gas. To clarify whether the negative correlation between SFE and M_* is attributed to the change in X_{CO} or that in true SFE, an independent determination of X_{CO} [e.g., simultaneous solving the CO-to- H_2 conversion factor and

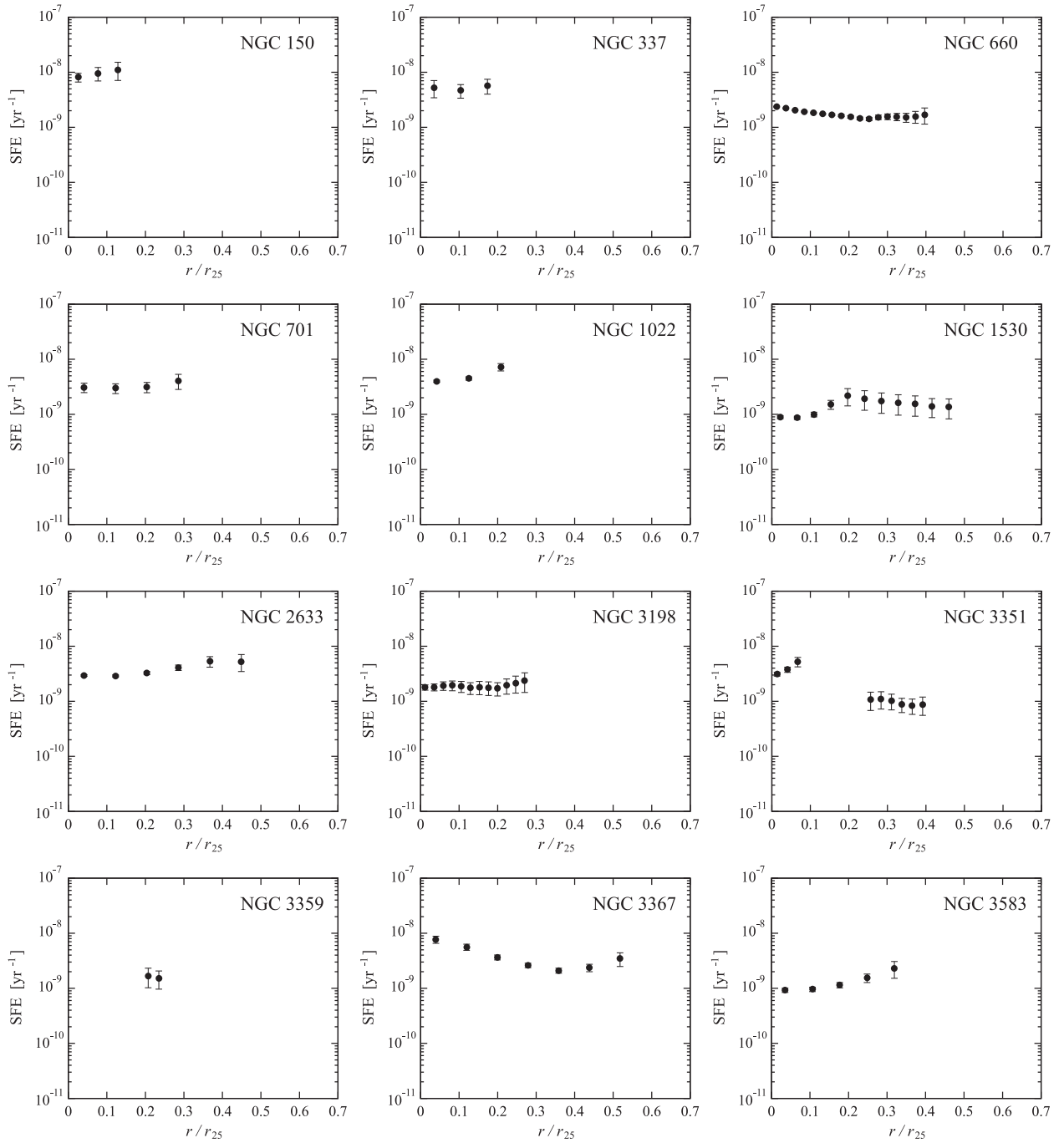


Fig. 5. SFE as a function of the galactocentric radius in the unit of r/r_{25} for individual SB galaxies.

dust-to-gas ratio proposed by Sandstrom et al. (2013)] in each galaxy and its comparison with the observed SFE are necessary.

4.2 Is SFE within the inner radii of SB galaxies intrinsically high?

Since the dependence of SFE on M_* has been confirmed, we try to cancel it and to evaluate the residual of the SFE. We

examined the $\log \text{SFE} - \log M_*$ relation by the ordinary least-squares power-law fit without uncertainties, and obtained the expression of $\log \text{SFE}_{\text{fit}} = -0.424 (\log M_*) - 4.31$. Then, we define the residual of SFE within the inner radii ($r/r_{25} < 0.3$) as

$$\Delta(\log \text{SFE}) = \log \text{SFE}_{\text{obs}} - \log \text{SFE}_{\text{fit}}, \quad (3)$$

where SFE_{obs} is the observed SFE. Figure 10 shows the comparison between $\Delta(\log \text{SFE})$ and M_* . Most of the galaxies

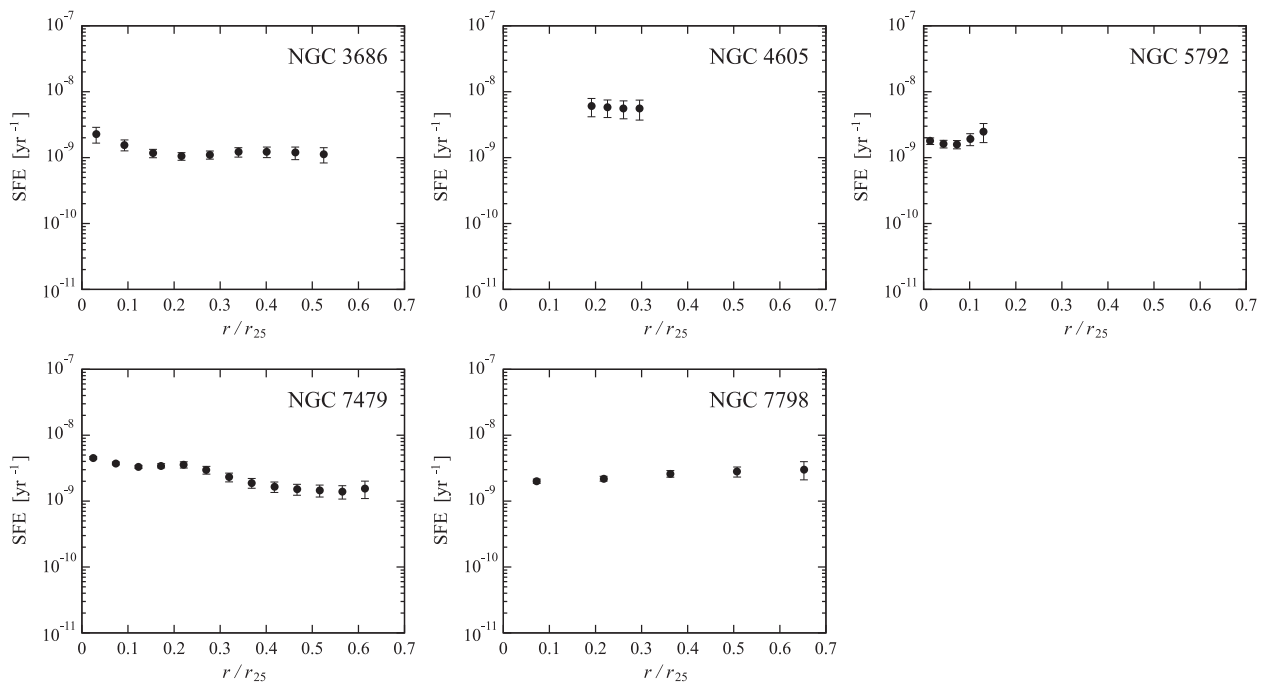
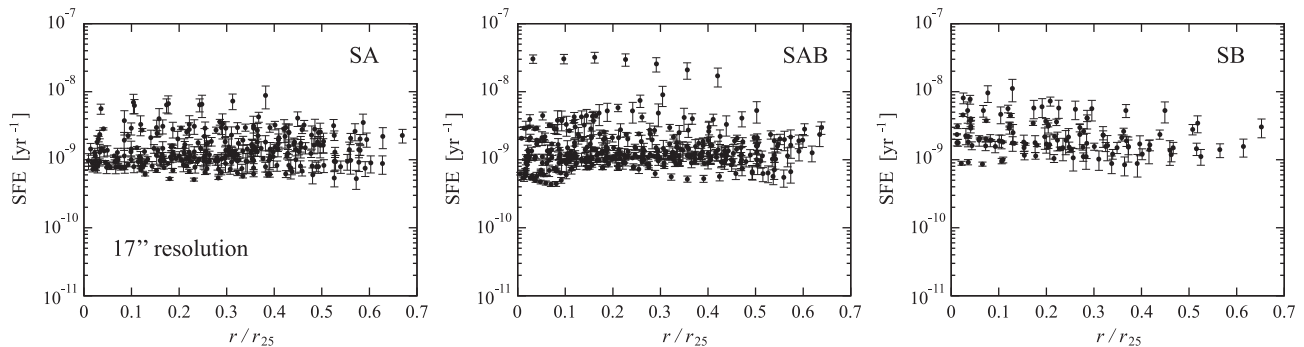


Fig. 5. (Continued)

Fig. 6. Compiled radial profiles in SFE at a common angular resolution of $17''$ for SA, SAB, and SB galaxies.

are within the $\Delta(\log \text{SFE})$ range of ± 0.5 . In order to make the distribution of $\Delta(\log \text{SFE})$ more visible, we examine histograms of $\Delta(\log \text{SFE})$ for each galaxy type as shown in figure 11. The frequency distributions of SA and SAB galaxies seem quite similar to each other, whereas that for SB galaxies seems offset from the high-SFE side compared to SA and SAB galaxies.

To evaluate whether the frequency distributions of $\Delta(\log \text{SFE})$ are different among SA, SAB, and SB galaxies, we examine two-sample Kolmogorov–Smirnov (K–S) tests. The K–S test between SA and SAB galaxies gives a p value of 0.51, and thus the hypothesis that the two samples originate from the same distribution is not rejected. However,

the K–S test between SAB and SB galaxies gives a p value of 0.037². This means the hypothesis that SAB and SB samples originate from the same distribution is rejected with a 95% confidence interval, suggesting that the SFE within the inner radii ($r/r_{25} < 0.3$) of SB galaxies is significantly higher than that within SA and SAB galaxies even though the dependence of SFE on M_* is cancelled.

Generally, stellar bars in galaxies can efficiently transport a large amount of molecular gas toward central regions (e.g., Matsuda & Nelson 1977; Simkin et al. 1980; Sakamoto et al. 1999; Haan et al. 2009), which

² The K–S test between SA and SB galaxies gives a p value of 0.024.

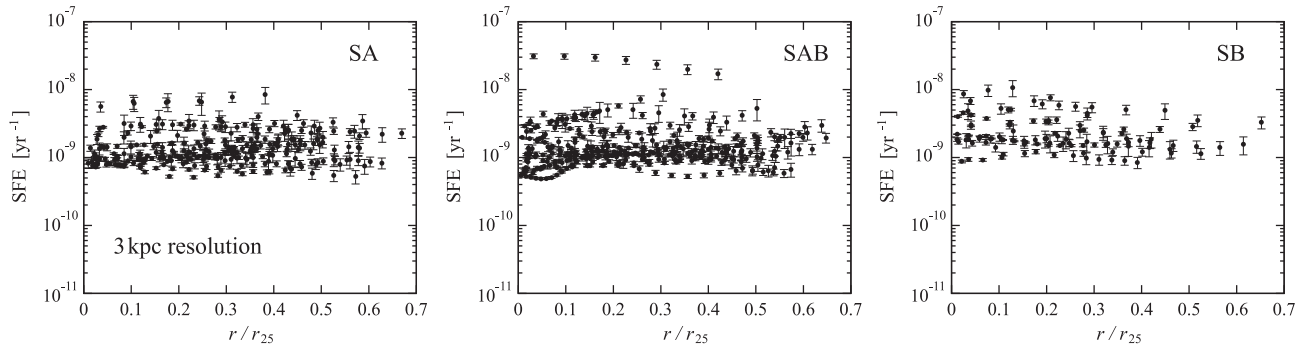


Fig. 7. Compiled radial profiles in SFE at a common spatial resolution of 3 kpc for SA, SAB, and SB galaxies.

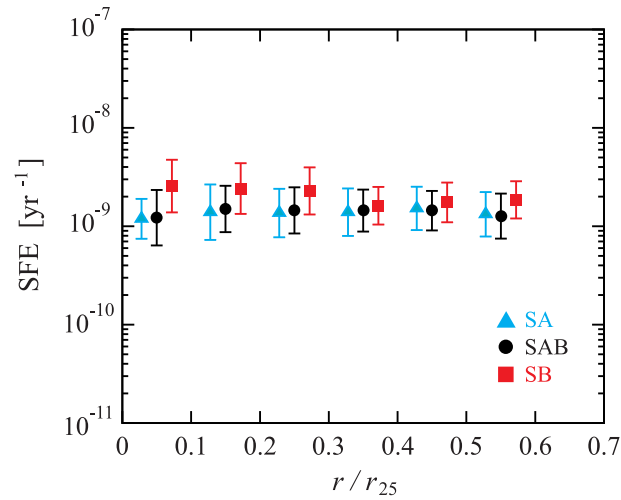


Fig. 8. Same as figure 6, but SFE is averaged over a $0.1r_{25}$ width. Blue triangles, black circles, and red squares indicate SA, SAB, and SB galaxies, respectively. In order to make the difference in SFE among galaxy types more visible, data points for SA and SB galaxies in each bin are offset to the left- and the right-hand sides, respectively. The error bars indicate the scatter of data points shown in figure 6.

invokes a nuclear star formation (e.g., Jogee et al. 2005; Schinnerer et al. 2006). Since SB galaxies typically have strong bars, high-SFE nuclear star formation (i.e., starburst) likely occurs in SB galaxies. However, the spatial scale of the nuclear star formation in nearby galaxies is typically in the range of a few $\times 100$ pc to 1 kpc (e.g., Kohno et al. 1999; Schinnerer et al. 2006; Muraoka et al. 2009), which corresponds to $r/r_{25} \sim 0.1$ or less. It seems that such a bursty star formation should occur even in the disk region to explain the high SFE toward $r/r_{25} \sim 0.3$.

Note that increasing the sample galaxies could affect our results; if only an SB galaxy with $\Delta(\log \text{SFE}) = 0$ is added to our sample, the p value of the K-S test between SAB and SB galaxies increases up to 0.058, which means that the null hypothesis is not rejected. Therefore, it is important to increase the number of SB galaxies for a more robust understanding of the difference in SFE among galaxy types.

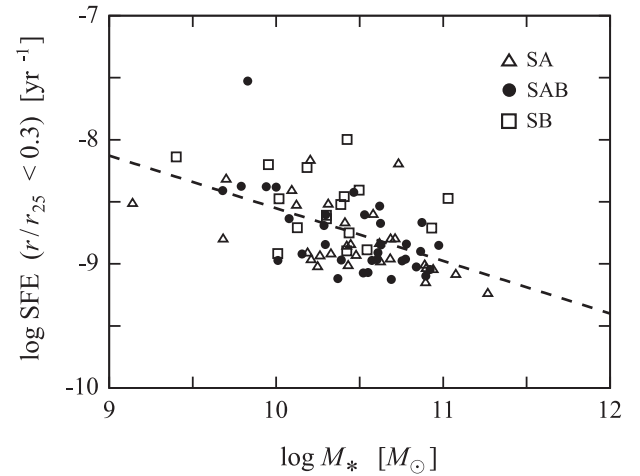


Fig. 9. Comparison between SFE within the inner radii ($r/r_{25} < 0.3$) and M_* in our sample. Open triangles, filled circles, and open squares indicate SA, SAB, and SB galaxies, respectively. The dashed line indicates the ordinary least-squares power-law fit for all the data points, which is expressed as $\log \text{SFE}_{\text{fit}} = -0.424(\log M_*) - 4.31$.

4.3 High SFE in the bar of SB galaxies

In order to investigate the physical origin of the high SFE within the inner radii ($r/r_{25} < 0.3$) further, we examine SFE maps for two representative SB galaxies in our sample, NGC 3367 and NGC 7479, as shown in figure 12. The ellipse of $r/r_{25} = 0.3$ seems to cover not only the central region but also a part of the disk, mainly the bar. For NGC 3367, we found that SFEs are $(5-8) \times 10^{-9} \text{ yr}^{-1}$ in the central region, $(2-4) \times 10^{-9} \text{ yr}^{-1}$ at r/r_{25} of 0.1–0.3 (corresponding to the bar), and $(1-2) \times 10^{-9} \text{ yr}^{-1}$ at $r/r_{25} > 0.3$ (corresponding to spiral arms) with the typical uncertainty of $0.5 \times 10^{-9} \text{ yr}^{-1}$. This indicates that the SFE in the bar is lower than that in the central region, but higher than in the spiral arms. A similar trend is found in NGC 7479; SFEs are $(3-6) \times 10^{-9} \text{ yr}^{-1}$ in the central region, $(3-6) \times 10^{-9} \text{ yr}^{-1}$ at the northern bar, $(1-2) \times 10^{-9} \text{ yr}^{-1}$ at the southern bar, and $(0.5-2) \times 10^{-9} \text{ yr}^{-1}$ in the spiral arms with the typical uncertainty of $0.3 \times 10^{-9} \text{ yr}^{-1}$.

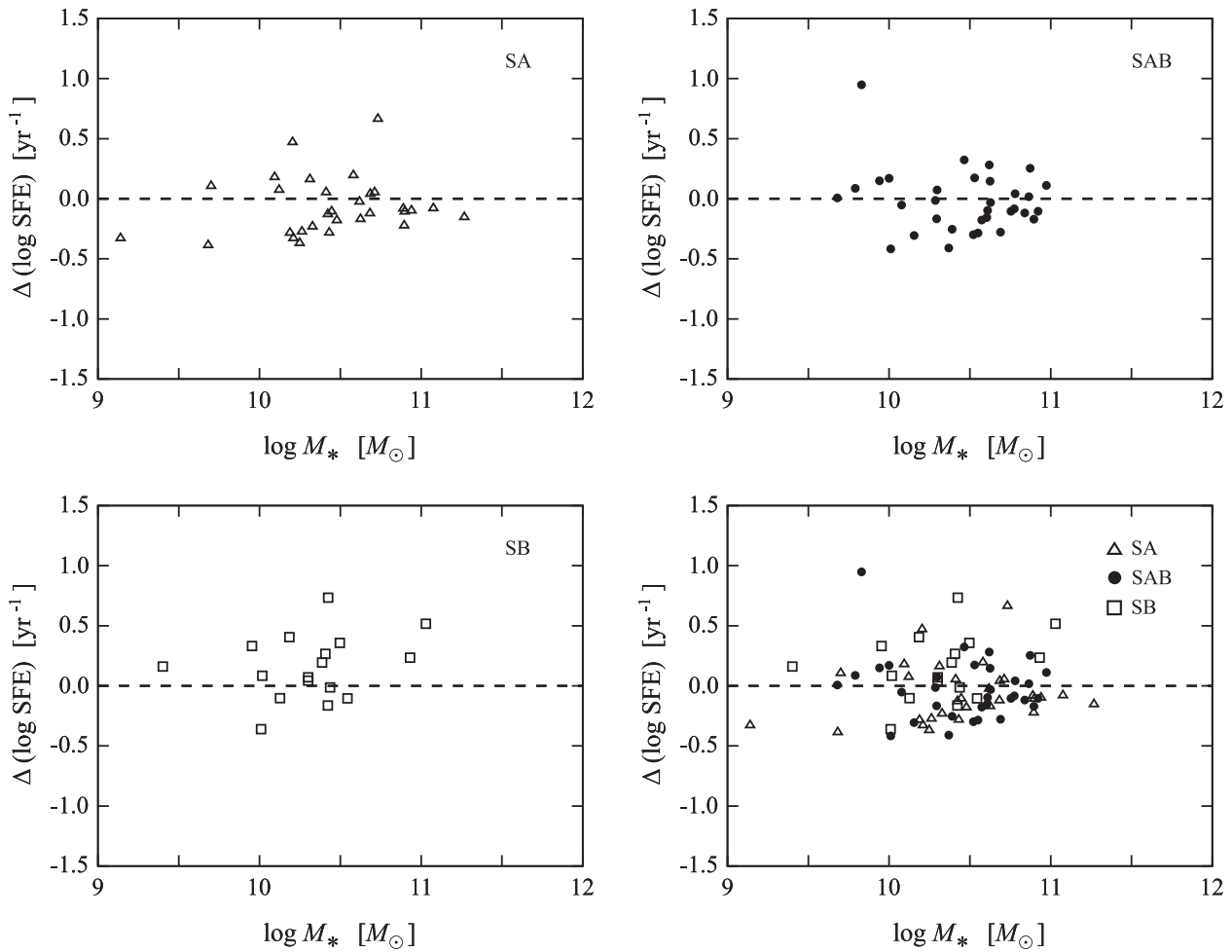


Fig. 10. Comparison between $\Delta(\log \text{SFE})$ and M_* . The dashed line indicates $\Delta(\log \text{SFE}) = 0$. Most of the galaxies are within the $\Delta(\log \text{SFE})$ range of ± 0.5 .

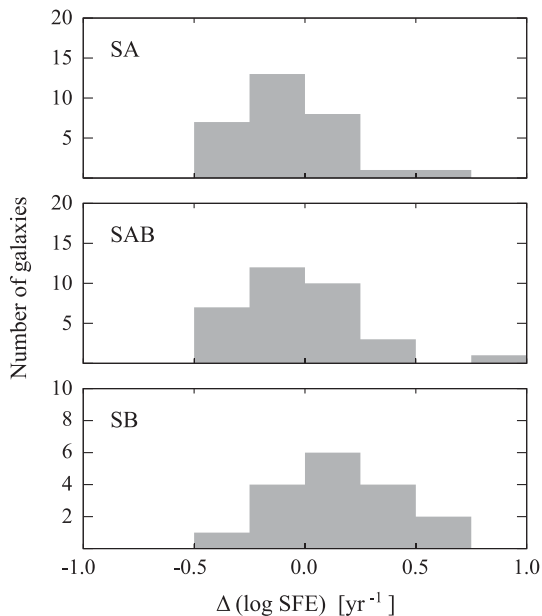


Fig. 11. Histograms of $\Delta(\log \text{SFE})$ for SA, SAB, and SB galaxies.

At least some of the SB galaxies in our sample show higher SFE in the bar than in the spiral arms. However, earlier studies reported an opposite trend in nearby barred spiral galaxies; SFE is lower in the bar than in the spiral arms (e.g., Momose et al. 2010; Watanabe et al. 2011; Hirota et al. 2014; Yajima et al. 2019). Here, we compare our SFE in NGC 4303 with that reported by Momose et al. (2010). They adopted a bar radius of $40''$ in NGC 4303, which corresponds to an r/r_{25} of 0.2. Thus we examine the averaged SFE, separating the NGC 4303 disk into an inner part ($r/r_{25} < 0.2$) and an outer part ($r/r_{25} > 0.2$). We obtain an averaged SFE in the inner part of $(8.4 \pm 0.9) \times 10^{-10} \text{ yr}^{-1}$ and that in the outer part of $(1.2 \pm 0.1) \times 10^{-9} \text{ yr}^{-1}$ (see figure 2); i.e., the SFE in the bar is ~ 1.4 times lower than that in the spiral arms. This trend is consistent with Momose et al. (2010), but opposite to what occurs in NGC 3367 and NGC 7479. Eventually, our results suggest that some barred spiral galaxies surely show lower SFE in the bar than in the spiral arms as reported by earlier studies, whereas this trend is not always true for other barred spiral

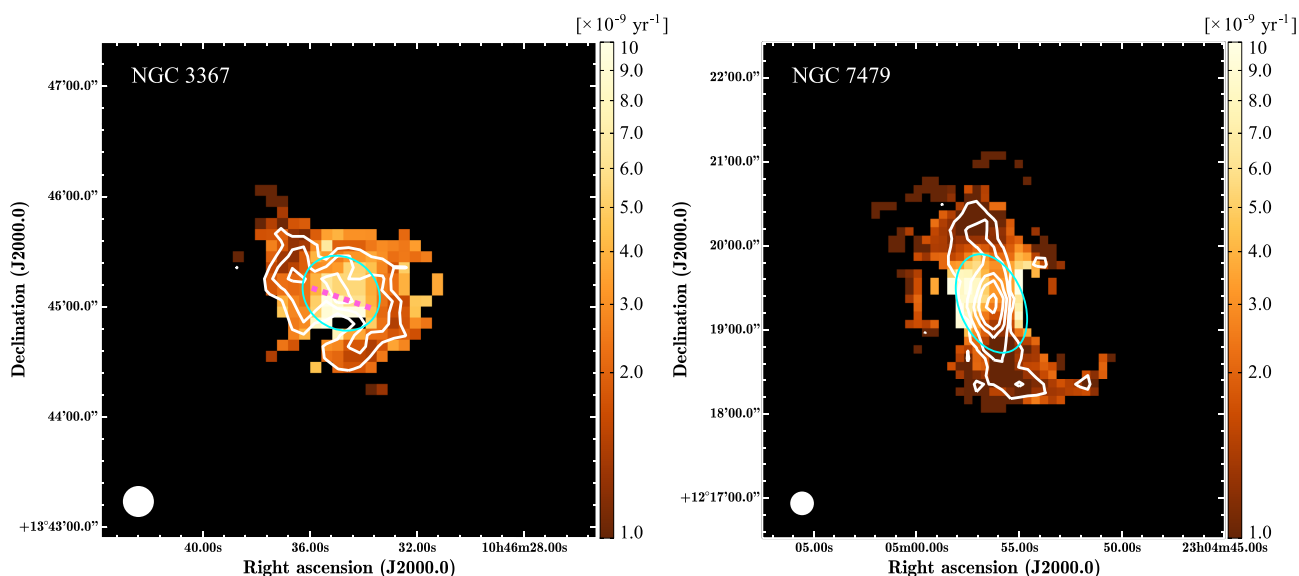


Fig. 12. Maps of SFE (color) superposed on the $^{12}\text{CO}(J = 1-0)$ integrated intensity obtained by COMING (white contour) in NGC 3367 (left) and NGC 7479 (right). The contour levels are 3, 6, and 10 K km s^{-1} for NGC 3367 and 5, 10, 20, 30, and 50 K km s^{-1} for NGC 7479, respectively. The blue ellipse indicates $r/r_{25} = 0.3$. The white circle at the bottom left-hand corner indicates the angular resolution of the maps, $17''$. The dashed magenta line in NGC 3367 indicates the position of the bar.

galaxies. In other words, there might be diversity of star formation activities in the bar.

Some mechanisms that suppress star formation in the bar have been already proposed. Generally, strong shocks and shear induced by the non-circular motion in the bar suppress the formation of dense molecular gas and massive stars, and thus SFE becomes lower in the bar compared to spiral arms (e.g., Reynaud & Downes 1998). In addition, recent numerical simulations suggest that star formation is enhanced by cloud–cloud collisions at moderate velocity ($15\text{--}40 \text{ km s}^{-1}$), which typically occur in spiral arms, but is rather suppressed by those at high velocity ($>60 \text{ km s}^{-1}$), which often occur in the bar (Fujimoto et al. 2014). This eventually causes lower SFE in the bar than in the spiral arms. In fact, the latest CO observations confirmed that the velocity dispersion of molecular gas, which would be an indicator of the collision velocity of clouds, is larger in the bar than in the spiral arms (e.g., Maeda et al. 2018; Yajima et al. 2019).

It is difficult to explain the physical origin of the high SFE in the bar, but a hint is provided by Zhou, Cao, and Wu (2015). They reported that barred galaxies with intense star formation in bars tend also to have active star formation in their bulges and disks. This suggests a possibility that a bar-driven process enhances SFE not only in the central region but also in the bar, although the specific physical mechanism to enhance star formation in the bar is unclear yet.

Note that we have to consider why SFEs of SA and SAB galaxies are similar to each other in all the radii although there is a distinct difference between the two types; existence

or non-existence of the bar. According to the explanation for the higher SFE in SB galaxies than in SAB galaxies as described above, we probably observe higher SFE in SAB galaxies than in SA galaxies because SAB galaxies have bars. In fact, earlier studies reported that the degree of molecular-gas concentration to the central kiloparsec is higher in barred galaxies than in non-barred galaxies (e.g., Sakamoto et al. 1999; Kuno et al. 2007).³ This suggests that intense star formation with high SFE occurs in the central regions of SAB galaxies as well as SB galaxies, whereas our results do not support such a simple scenario.

In order to solve such complications regarding the difference in SFE within the inner radii among SA, SAB, and SB galaxies, formation processes of dense gas and massive stars in the bar should be investigated further. In particular, it is essential to understand dynamical effects such as cloud–cloud collisions, shocks, and shear because they play a key role in enhancement or suppression of star formation. In addition, the measurement of fractional mass of the dense gas in molecular gas (f_{DG}) is important. Torii et al. (2019) examined f_{DG} in the Milky Way using ^{12}CO and C^{18}O molecules, and found that f_{DG} in the Galactic arms is as high as $\sim 4\%\text{--}5\%$, while it becomes quite small, $0.1\%\text{--}0.4\%$, in the Galactic bar and inter-arm regions. Such a

³ In the Sakamoto et al. (1999) sample, nine out of 10 barred galaxies are classified as SAB type, and 24 out of 28 barred galaxies are SAB type in the Kuno et al. (2007) sample. Thus we can read their studies as a comparison between SA and SAB galaxies.

study of f_{DG} and its relation to dynamical effects can be conducted for external galaxies with high-sensitivity and high-angular-resolution observations. The latest interferometers, such as the Atacama Large Millimeter/submillimeter Array and the Northern Extended Millimeter Array, are certainly helpful for furthering the understanding of the star formation in the bar.

5 Summary

We examined radial variations in molecular-gas based SFE for 80 galaxies selected from the COMING sample. A summary of this work is as follows.

- (1) We found that the radial variations in SFE for individual galaxies are typically a factor of 2–3, which suggests that SFE is nearly constant along galactocentric radius.
- (2) We found the averaged SFE in 80 galaxies of $(1.69 \pm 1.1) \times 10^{-9} \text{ yr}^{-1}$, which is consistent with Leroy et al. (2008) if we consider the contribution of helium to the molecular gas mass evaluation and the difference in the assumed initial mass function between the two studies.
- (3) Within the inner radii ($r/r_{25} < 0.3$), the SFE of SB galaxies ($>2.0 \times 10^{-9} \text{ yr}^{-1}$) is significantly higher than that of SA and SAB galaxies ($\sim 1.4 \times 10^{-9} \text{ yr}^{-1}$). This trend can be partly explained by the dependence of SFE on global stellar mass, which probably relates to X_{CO} through the metallicity. According to the K–S test, however, we found that SFE within the inner radii of SB galaxies is still higher than that of SA and SAB galaxies even though the dependence of SFE on M_* is cancelled.
- (4) For two representative SB galaxies in our sample, NGC 3367 and NGC 7479, the ellipse of $r/r_{25} = 0.3$ seems to cover not only the central region but also a part of the disk, mainly the bar. These two galaxies show higher SFE in the bar than in the spiral arms. However, we found an opposite trend in NGC 4303; SFE is lower in the bar than in the spiral arms, which is consistent with earlier studies (e.g., Momose et al. 2010). These results suggest a diversity of star formation activities in the bar.

Acknowledgments

We thank the referee for invaluable comments, which significantly improved the manuscript. We are indebted to the NRO staff for the commissioning and operation of the 45 m telescope and their continuous efforts to improve the performance of the instruments. This work is based on observations at NRO, which is a branch of the National Astronomical Observatory of Japan, National Institutes of Natural Sciences. This research has made use of the NASA/IPAC Extragalactic Database, which is operated by the Jet Propulsion Laboratory, California Institute of Technology, under contract with the National Aeronautics and Space Administration. This work was supported by JSPS KAKENHI (Grant Nos. 17K14251, 17H01110, and 18J00508).

References

- Arimoto, N., Sofue, Y., & Tsujimoto, T. 1996, PASJ, 48, 275
 Bigiel, F., et al. 2011, ApJ, 730, L13
 Bolatto, A. D., Wolfire, M., & Leroy, A. K. 2013, ARA&A, 51, 207
 Boselli, A., Cortese, L., Boquien, M., Boissier, S., Catinella, B., Lagos, C., & Saintonge, A. 2014, A&A, 564, A66
 Cardelli, J. A., Clayton, G. C., & Mathis, J. S. 1989, ApJ, 345, 245
 Casasola, V., et al. 2017, A&A, 605, A18
 Daddi, E., et al. 2010, ApJ, 714, L118
 Dib, S., Piau, L., Mohanty, S., & Braine, J. 2011, MNRAS, 415, 3439
 Fujimoto, Y., Tasker, E. J., & Habe, A. 2014, MNRAS, 445, L65
 Gilde Paz, A., et al. 2007, ApJS, 173, 185
 Haan, S., Schinnerer, E., Emsellem, E., García-Burillo, S., Combes, F., Mundell, C. G., & Rix, H.-W. 2009, ApJ, 692, 1623
 Hatakeyama, T., et al. 2017, PASJ, 69, 67
 Hirota, A., et al. 2014, PASJ, 66, 46
 Huang, M.-L., & Kauffmann, G. 2014, MNRAS, 443, 1329
 Hughes, T. M., Cortese, L., Boselli, A., Gavazzi, G., & Davies, J. I. 2013, A&A, 550, A115
 Jarrett, T. H., et al. 2011, ApJ, 735, 112
 Jøgee, S., Scoville, N., & Kenney, J. D. P. 2005, ApJ, 630, 837
 Kennicutt, R. C., Jr, 1998, ARA&A, 36, 189
 Kohno, K., Kawabe, R., & Vila-Vilaró, B. 1999, ApJ, 511, 157
 Kroupa, P. 2001, MNRAS, 322, 231
 Kuno, N., et al. 2007, PASJ, 59, 117
 Lequeux, J., Peimbert, M., Rayo, J. F., Serrano, A., & Torres-Peimbert, S. 1979, A&A, 80, 155
 Leroy, A. K., et al. 2013, AJ, 146, 19
 Leroy, A. K., Walter, F., Brinks, E., Bigiel, F., de Blok, W. J. G., Madore, B., & Thornley, M. D. 2008, AJ, 136, 2782
 Lisenfeld, U., et al. 2011, A&A, 534, A102
 Maeda, F., Ohta, K., Fujimoto, Y., Habe, A., & Baba, J. 2018, PASJ, 70, 37
 Matsuda, T., & Nelson, A. H. 1977, Nature, 266, 607
 McKee, C. F., & Ostriker, E. C. 2007, ARA&A, 45, 565
 Minamidani, T., et al. 2016, SPIE Proc. , 9914, 99141Z
 Miralles-Caballero, D., Díaz, A. I., Rosales-Ortega, F. F., Pérez-Montero, E., & Sánchez, S. F. 2014, MNRAS, 440, 2265
 Momose, R., Okumura, S. K., Koda, J., & Sawada, T. 2010, ApJ, 721, 383
 Muraoka, K., et al. 2007, PASJ, 59, 43
 Muraoka, K., et al. 2009, PASJ, 61, 163
 Muraoka, K., et al. 2016, PASJ, 68, 89
 Pastoriza, M. G., Dottori, H. A., Terlevich, E., Terlevich, R., & Diaz, A. I. 1993, MNRAS, 260, 177
 Reynaud, D., & Downes, D. 1998, A&A, 337, 671
 Saintonge, A., et al. 2011, MNRAS, 415, 61
 Sakamoto, K., Okumura, S. K., Ishizuki, S., & Scoville, N. Z. 1999, ApJ, 525, 691
 Salpeter, E. E. 1955, ApJ, 121, 161
 Sandstrom, K. M., et al. 2013, ApJ, 777, 5
 Schinnerer, E., Böker, T., Emsellem, E., & Lisenfeld, U. 2006, ApJ, 649, 181
 Schlafly, E. F., & Finkbeiner, D. P. 2011, ApJ, 737, 103

- Simkin, S. M., Su, H. J., & Schwarz, M. P. 1980, *ApJ*, 237, 404
- Sorai, K., et al. 2019, *PASJ*, 71, S14
- Torii, K., et al. 2019, *PASJ*, 71, S2
- Tremonti, C. A., et al. 2004, *ApJ*, 613, 898
- Utomo, D., et al. 2017, *ApJ*, 849, 26
- Watanabe, Y., Sorai, K., Kuno, N., & Habe, A. 2011, *MNRAS*, 411, 1409
- Wen, X.-Q., Wu, H., Zhu, Y.-N., Lam, M. I., Wu, C.-J., Wicker, J., & Zhao, Y.-H. 2013, *MNRAS*, 433, 2946
- Wright, E. L., et al. 2010, *AJ*, 140, 1868
- Yajima, Y., et al. 2019, *PASJ*, 71, S13
- Young, J. S., Allen, L., Kenney, J. D. P., Lesser, A., & Rownd, B. 1996, *AJ*, 112, 1903
- Zhou, Z.-M., Cao, C., & Wu, H. 2015, *AJ*, 149, 1